Changes to extreme wave climates of islands within the Western Tropical Pacific throughout the 21st century under RCP 4.5 and RCP 8.5, with implications for island vulnerability and sustainability

James B. Shope [a,*], Curt D. Storlazzi [b], Li H. Erikson [b], Christie A. Hegermiller [c]

[a] University of California at Santa Cruz, Earth and Planetary Sciences, 1156 High Street, Santa Cruz, CA 95065, USA
[b] US Geological Survey, Pacific Coastal and Marine Science Center, 400 Natural Bridges Drive, Santa Cruz, CA 95060, USA
[c] University of California at Santa Cruz, Ocean Sciences, 1156 High Street, Santa Cruz, CA 95065, USA

ABSTRACT

Waves are the dominant influence on coastal morphology and ecosystem structure of tropical Pacific islands. Wave heights, periods, and directions for the 21st century were projected using near-surface wind fields from four atmosphere–ocean coupled global climate models (GCM) under representative concentration pathways (RCP) 4.5 and 8.5. GCM-derived wind fields forced the global WAVEWATCH-III wave model to generate hourly time series of bulk wave parameters around 25 islands in the mid to western tropical Pacific Ocean for historical (1976–2005), mid-century, and end-century time periods for the December–February and June–August seasons. The December–February regional wave climate is dominated by strong winds and large swell from extratropical cyclones in the north Pacific while the June–August season brings smaller waves generated by the trade winds and swell from Southern Hemisphere extratropical storms. Extreme significant wave heights decreased (~10.0%) throughout the 21st century under both climate scenarios compared to historical wave conditions and the higher radiative forcing RCP 8.5 scenario displayed a greater and more widespread decrease in extreme significant wave heights compared to the lower forcing RCP 4.5 scenario. An exception was for the end-century June–August season. Offshore of islands in the central equatorial Pacific, extreme significant wave heights displayed the largest changes from historical values. The frequency of extreme events during December–February decreased under RCP 8.5, whereas the frequency increased under RCP 4.5. Mean wave directions rotated more than 30° clockwise at several locations during June–August, which could indicate a weakening of the trade winds' influence on extreme wave directions and increasing dominance of Southern Ocean swell. The results of this study underscore that December–February large wave events will become smaller and less frequent in most regions, reducing the likelihood and magnitude of wave-driven flooding at these island locations over the 21st century. However, relatively large increases in the mean of the top 5% of significant wave heights and large changes to the mean direction of these waves in the June–August season at several islands within 150–180° E will drive greater flooding and island morphological change along previously more stable shorelines. The reported results herein project large changes to tropical Pacific island wave climates that will be necessary for assessing island vulnerability under climate change in future studies.

Published by Elsevier B.V.

1. Introduction

Large wave events generated from tropical and extratropical cyclones pose a significant threat to low-lying Pacific island nations. Flooding from these events can damage infrastructure, salinate groundwater, and ruin crops; the waves can induce large morphological changes to island coastlines (Terry and Falkland, 2010; Aucan et al., 2012; Hoeke et al., 2013; Smithers and Hoeke, 2014). It is anticipated that sea-level rise (SLR) will increase the severity of flooding events, as more wave energy will reach the shoreline (Nicholls et al., 2007;

Storlazzi et al., 2011; Seneviratne et al., 2012). However, these SLR projections do not take changing wave climates into account. Understanding how the magnitude and frequency of large wave events will change over the next century is critical to anticipate hazards to island communities and changes to island morphology.

Previous research projecting the stability and sustainability of tropical Pacific islands (Dickinson, 1999; Woodroffe, 2008; Webb and Kench, 2010) has predominantly focused on inundation from SLR. Sea level in the western tropical Pacific (WTP) rose at a rate of 4.3 mm/yr over 1993–2001, which is significantly faster than the global average of approximately 3.0 mm/yr (Church et al., 2006, 2013). Increased SLR rates in the WTP are associated with increased regional trade wind intensity (Merrifield, 2011; Merrifield and Maltrud, 2011). If SLR in the

* Corresponding author.
E-mail address: jshope@ucsc.edu (J.B. Shope).

WTP continues at a fast rate, the region will likely experience more extensive inundation in the near future. However, extreme wave events coupled with SLR will threaten island communities before inundation by SLR alone, as increased sea level will contribute to extreme high water levels along coasts, allowing nearshore waves to be larger and more damaging (Seneviratne et al., 2012).

Global (Hemer et al., 2013; Mori et al., 2013) and regional (Semedo et al., 2013) projections of future WTP wave conditions show general decreases in boreal winter (December–February) and summer (June–August) significant wave heights (H_s) by the end of the 21st century. These projections, however, focus on mean wave parameters instead of extreme events. There has been limited exploration of global extreme wave conditions, but recent studies forecast decreases in Pacific extreme H_s (Fan et al., 2013; Wang et al., 2014). Regional-scale projected extremes are still uncertain, yet Pacific island nations are increasingly threatened by SLR and depend on these projections as extreme events deliver the most devastating impacts to insular communities and island morphologies (Fletcher and Richmond, 2010; Hoeke et al., 2013).

Many extreme wave events within the WTP are dominated by swell waves generated by extratropical cyclones (Hoeke et al., 2013). In December 2008, an extreme event inundated five island nations in the tropical Pacific over a period of several days, resulting in significant damage to community infrastructure and large-scale coastal erosion (Fletcher and Richmond, 2010; Smithers and Hoeke, 2014). However, there have been few studies projecting how waves from extratropical storms within the WTP will change over the 21st century and how these changes may affect island nations in the region. Combined with King tides (maximum annual spring high tides), El Niño Southern Oscillation (ENSO)–induced seasonal sea level anomalies, and/or tropical cyclone storm surge, extratropical cyclone waves can deliver even more energy to island shorelines via reduced depth-limited breaking (Storlazzi et al., 2011; Seneviratne et al., 2012; Hoeke et al., 2013). Therefore, extratropical swell has the potential to cause significant flooding events along low-elevation Pacific island coastlines throughout the WTP.

In this paper, we present results derived from near-surface wind fields from four Coupled Model Intercomparison Project, phase 5 (CMIP5) global climate models (GCMs) used to force WAVEWATCH-III (WW3) to project wave conditions in the WTP. Projections of December–February (DJF) and June–August (JJA) parameters of the mean of the top 5% of significant wave heights were developed for historical (1976–2005), mid-century (2026–2045), and end-century (2081–2100) time periods. This study focused primarily on waves generated in extratropical regions. These extratropical-generated swell waves, although likely smaller than typhoon-generated waves, will pose a hazard to these islands throughout the 21st century as SLR enables more extensive flooding. A description of the study area's wave climatology and island vulnerability is given in Section 2. Section 3 details the GCM and WW3 input parameters and analysis methods. Section 4 presents the model skill analysis, changes in wind speed conditions, and extreme wave parameters (heights, directions, and frequencies) relative to historical values. Wave parameter changes during DJF and JJA for the mid- and end-century are presented separately. A discussion of implications to island vulnerability from these changes is presented in Section 5 and conclusions in Section 6.

2. Study area

2.1. Wave and Wind Climate

This study focused on 25 island locations in the tropical Pacific west of 150° W (Fig. 1a) that were divided into six regions based on proximity and similarity of general atmospheric patterns (Australian Bureau of Meteorology and CSIRO, 2014): Western, Marianas, Central, Northeast, Eastern Equatorial, and Southern (Fig. 1b). WTP H_s are generally larger and more energetic during boreal winter than during other seasons
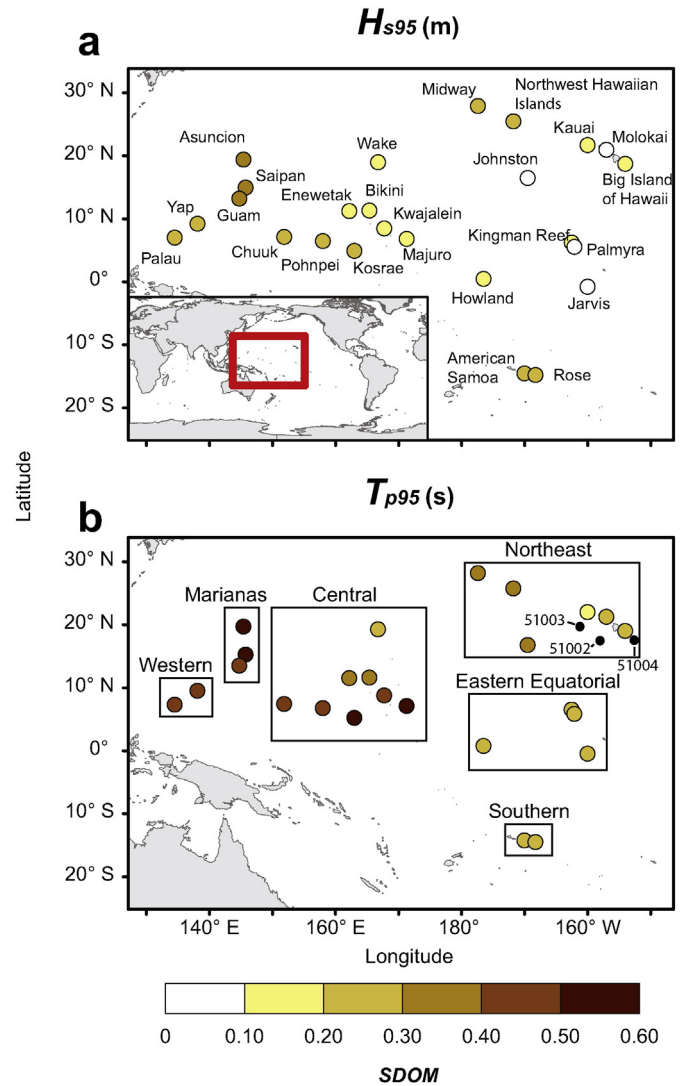

Fig. 1. Extent map of the study area displaying model coherence over the hindcasted period (1976–2005). (a) H_{s95} and (b) T_{p95}. The colors represent the magnitude of the standard deviation of the mean (SDOM) for (a.) H_{s95} and (b.) T_p of H_{s95} values. The red box in (a) indicates the study area within the global map. Black boxes in (b) represent regional groupings of output points based on proximity and similar variation. Black points in (b) represent National Data Buoy Center station names and locations near the Hawaiian Islands.

(Young, 1999; Bromirski et al., 2013). Swell generated by northern hemisphere extratropical cyclones dominates the extreme wave climate of the WTP during boreal winters and summers. Boreal winter waves are generally the largest in the region each year, except for the Southern Hemisphere islands, where waves are largest during the boreal summer (Young, 1999). These waves can traverse more than 4000 km within the basin, delivering energy from mid-latitude cyclones to islands near the equator (Hoeke et al., 2013). During boreal summer, waves generated by easterly trade winds dominate the swell wave spectrum in the eastern half of the study area. Waves generated in the Southern Hemisphere characterize larger swell waves in the western half of the region during the boreal summer (Young, 1999; Australian Bureau of Meteorology and CSIRO, 2014).

Easterly trade winds dominate atmospheric circulation and surface winds within the region throughout most of the year (Australian Bureau of Meteorology and CSIRO, 2014). However, the strongest winds in the region are the result of tropical cyclones and other storm systems. The northeast quadrant of the study area receives strong winds and large waves from mid-latitude storms during boreal winter, despite the

influence of the trade winds (Vitousek and Fletcher, 2008; Semedo et al., 2011). Extreme winds and waves in the western half of the study area are mainly from typhoons and mid-latitude extratropical cyclones (Mori et al., 2010).

2.2. Island characteristics and vulnerability

Two primary island types are found within this region: volcanic "high" islands and low-altitude atoll islands. Though most high islands, such as the Mariana and Main Hawaiian Islands, have high mean elevations (10 s–1000 s of m), their harbors, population centers, and infrastructure are generally concentrated along the coast within a few meters of sea level. These low-elevation areas are vulnerable to large wave events (Mimura, 1999). Many high islands in the tropical Pacific have fringing reefs along their coasts that function as breakwaters for incident waves, protecting coastal areas from larger waves and reducing wave-driven flooding (Ferrario et al., 2014). Coastal groundwater on high islands can become salinated from flooding, but large abundances of fresh groundwater generally flush contaminated water out of the aquifer quickly (Rotzoll and Fletcher, 2012).

Atoll islands, such as the Marshall or Northwestern Hawaiian Islands, are low-lying carbonate islands on atoll reefs that generally have mean elevations of less than 2–3 m above sea level. They have high population densities (e.g., 8300 people/km^2 on Fongafale, Tuvalu) and represent most of the inhabited landmass in the tropical Pacific (Webb and Kench, 2010; Ford, 2012). Due to their low elevation, many atoll islands are vulnerable to inundation, saltwater intrusion, enhanced shoreline erosion, and infrastructure damage due to wave-driven flooding events that will likely be exacerbated by SLR. However, it is unlikely that WTP atoll islands will be completely inundated in the future, as they are dynamic features with shorelines that change considerably over short time periods of days to years in response to changing wave patterns (Kench and Brander, 2006; Rankey, 2011; Beetham and Kench, 2014). Even so, the mechanism by which an atoll island can vertically accrete to keep up with SLR is for wave-driven flooding events to entrain sediment from the adjacent reefs and deposit it onshore. This overwash is beneficial to island growth over geologic timescales, but such wave-induced flooding events may make these islands inhospitable for humans over shorter time scales, due to impacts to infrastructure, agriculture, and freshwater resources (Mimura, 1999; Yamano et al., 2007; Fletcher and Richmond, 2010). Once salinated due to wave-driven overwash, freshwater lenses (the main source of freshwater on atoll islands) take on the order of months to years to completely refreshen, depending on precipitation and climate (Terry and Falkland, 2010). Therefore, the frequency of these events is concerning: if large wave events become more frequent over the next century, the slow freshening process may render freshwater lenses of atoll islands permanently unpotable.

2.3. Implication of Wave Changes to Island Vulnerability and Stability

The results of this study allow for a first-order evaluation of how changing extreme wave conditions from increased radiative forcing due to global climate change may impact processes that govern WTP island coastlines over the next century. It is therefore necessary to briefly outline how potential changes to incident waves can affect set-up, flooding, and erosional patterns along reef line shorelines. Deep-water wave heights serve as a proxy for wave energy reaching island shorelines after attenuation by coral reefs. Shoreline reefs induce depth-limited breaking of larger waves at the reef crest and flat, effectively dissipating as much as 97% of the total wave energy before it reaches shore and reducing incident wave heights up to 84% (Storlazzi et al., 2011; Ferrario et al., 2014). Although large waves may break offshore, a fraction of the energy still progresses towards shore, increasing the cross-shore radiation stress and driving set-up along the reef flat (Pequignet et al., 2011). Set-up from waves can increase local sea levels along

reef-protected island coasts by as much as 32% of breaking wave heights at reef crests (Pequignet et al., 2011; Merrifield et al., 2014). Pequignet et al. (2011) and Becker et al. (2014) found that set-up along reef flats was positively correlated with reef face breaking wave heights. Increased set-up on reef flats results from larger wave heights at the reef crest, reducing wave energy dissipation at the reef crest and allows more wave energy to be delivered to the shoreline. Therefore, although much wave energy is dissipated, larger wave heights and greater resulting set-ups deliver greater energy to shore, driving flooding and potential erosion of reef-protected coastlines (Storlazzi et al., 2011; Grady et al., 2013).

3. Methods

3.1. Global climate models and analyses

Recent historical and future wave conditions were generated for the western tropical Pacific Ocean via a dynamical downscaling approach (Wang et al., 2009). Four separate atmosphere–ocean coupled global climate model (GCM) wind fields under two climate change scenarios forced the WAVEWATCH-III (WW3) numerical wave model (ver. 3.14; Tolman et al., 2002; Tolman, 2009). The selected GCMs and their resolutions are listed in Table 1; all GCMs follow the CMIP5 framework (World Climate Research Programme, 2013). Three time periods were simulated: historical (1976–2005), mid-century (2026–2045), and end-century (2081–2100). Two IPCC–defined climate change scenarios forced the GCM runs: representative concentration pathway (RCP) 4.5 characterizes a medium increase of radiative forcing (4.5 W/m^2 by 2100 relative to preindustrial conditions) assuming stabilization starting mid-century, and RCP 8.5 characterizes unabated radiative forcing increase to 8.5 W/m^2 by 2100 relative to preindustrial conditions (Riahi et al., 2010; Thomson et al., 2011).

GCM-derived three-hourly wind speed and direction fields forced WW3 over a near-global domain (NWW3, latitude 80° S–80° N) at a 1.00° × 1.25° spatial resolution (Table 1). Bathymetry was generated from the Naval Research Laboratory's (2013) Digital Bathymetric Data Base version 3.0 and shoreline positions were generated with the National Geophysical Data Center's (2013) Global Self-consistent Hierarchical High-resolution Geography Database version 2.2.2. Wave spectra were computed in 25 frequency bands ranging from 0.04 to 0.50 Hz with a directional resolution of 15°. Nonlinear quadruplet wave interactions were modeled using the Hasselmann et al. (1985) formulation, and wave growth and whitecapping were simulated via the Tolman and Chalikov (1996) source term package. Diffraction and wind interruption from the small islands within the model domain were not resolved due to the coarse spatial resolution of the WW3 domain. This limitation was accounted for within this study by focusing on trends of offshore, deep water waves that are relatively unaffected by these smaller islands. The larger Hawaiian Islands were resolved, however, and the diffraction and wind effects were accounted for within WW3. Additionally, the effects of ENSO were not considered within this study. It appears that ENSO is only somewhat realistically represented in about half of all CMIP5 GCM models (Kim and Yu, 2012). Also, Stevenson (2012) noted that ENSO variability and amplitudes within 27 CMIP5 multi-model means under climate change projections were statistically indistinguishable from values determined for the 20th

Table 1
List of global climate models used, wave model used, and the model resolutions.

Model	Resolution (longitude × latitude) in degrees
BCC-CSM1.1	2.8 × 2.8
INM-CM4	2.0 × 1.5
MIROC5	1.4 × 1.4
GFDL-ESM2M	2.5 × 1.5
WAVEWATCHIII	1.25 × 1.00

century. In the few models where ENSO amplitudes do increase with climate change forcing under RCP 4.5, the changes were smaller than the standard deviation of ENSO amplitudes of all tested CMIP5 models (Kim and Yu, 2012). Due to the weak to non-existent changes to ENSO intensity with climate change in these studies, it can be assumed that ENSO did not change significantly within our model runs and affect wave parameters. Hourly time series of H_s, peak wave periods (T_p), and mean wave directions (D_m) were saved at 25 locations from WW3 runs. D_m is defined as the mean direction in which H_s propagates, measured in degrees clockwise from north. Outputs from each GCM-driven WW3 model run were concatenated into a multi-model dataset on monthly and seasonal scales. An ensemble of models better simulates observed data than any single model for dynamic GCMs and regional climate models with similar parameters (Donat et al., 2010).

Multi-model averages and standard deviations of boreal winter (DJF) and summer (JJA) extreme H_s, T_p, and D_m were calculated for historical, mid-century, and end-century periods. Extreme values are defined as the mean of the top 5% of H_s and associated T_p and D_m each season (those exceeded 36 h/month) over each time period (numbering 175,200 measurements for each future period and 262,800 measurements for the historical period). Seasonal (DJF or JJA) values were first taken from the complete model datasets; the extreme H_s and the T_p and D_m associated with those values were selected and combined into a multi-model extreme H_s value dataset from which seasonal averages were calculated. Extreme significant wave heights are denoted H_{s95}, with a standard deviation of σ_{Hs95}, and associated mean wave direction are denoted D_{m95}, with a standard deviation of σ_{Dm95}. D_{m95} was calculated by converting the wave directions of H_{s95} and H_{s95} magnitudes into rectangular (x, y) vectors and summing the resultant components. These components were then used in the formula: $D_{m95} =$ arctangent (Σy, Σx), where D_{m95} is the mean wave direction of the top 5% of significant wave heights, y is the north–south component of the wave directions in radians and x is the east–west component of the wave directions in radians. The average direction of waves is weighted by H_{s95} and the D_{m95} equation accounts for wave directions at 0° and 360° being the same. Peak wave periods associated with H_{s95} are designated as T_{p95}. Projections of boreal spring and fall seasons are beyond the scope of this report because the selected models do not fully capture tropical cyclones, the dominant wave generation mechanism during these seasons.

For both DJF and JJA, the frequency of extreme wave events with the greatest spectral energy density each season (extrapolated to events per decade, f_{ext}) was calculated, with a standard deviation of σ_f. The power spectrum was calculated for each season on a yearly basis using a Hanning window of 30 d with 50% overlap for each season (~90 d). The power spectrum was calculated by applying an infinite impulse response discrete fast Fourier transform digital filter to the seasonal time series of H_s values of each model year by year. From the Hanning windowed power spectrum, the frequency with the greatest energy density was recorded for each model and year (e.g., 30 years of historical simulations resulted in 120 separate measurements of frequencies as there were four separate GCM-forced WW3 simulations). These frequencies were then combined into multi-model averages for each location for each time period. The selected frequencies represent the events that deliver the most energy to these islands during each season and not the exceedances of a single threshold. Rather, the frequencies recorded were the ones that have the largest potential to drive morphological change within one season. Therefore, these frequencies do not necessarily represent the frequency of H_{s95} events. The dominant frequency of future and historical periods was subsequently derived for DJF and JJA for all GCM-driven WW3 runs. Data provided herein are relegated to deep-water wave conditions in the tropical Pacific, but changes in extreme wave heights, directions, and f_{ext} were broadly extrapolated to determine effects on the coastlines of atoll and volcanic islands in the tropical Pacific. For further detail on model parameters, model output, and bulk wave parameter analysis, refer to Storlazzi et al. (2015).

3.2. Model skill

Multi-model historical wave conditions were compared to National Data Buoy Center (NDBC) platform measurements at the same locations in the Hawaiian Island Chain (NDBC, 2013) to evaluate the skill of the models to approximate observed extreme wave climate. The Pacific Ocean historical buoy dataset is scattered, inconsistent, and temporally short. The Hawaiian Island Chain was the only location that had observation platforms (NDBC buoys 51001, 51003, and 51004; Fig. 1b) with sufficiently long datasets (data from 1985 to 2005 were used in this study) to compare with WW3 historical time series. Other buoys in the Pacific generally offered only a year or less of temporal overlap with the historical simulation period. The models do not approximate the observed H_s, T_p, and f_{ext} datasets on a year-by-year basis, but rather on a multi-annual scale, and therefore an error analysis using buoys offering only limited temporal overlap was not carried out. These NDBC buoys collect hourly deep-water H_s and T_p measurements. These buoys were co-located with WW3 Hawaiian virtual buoy output locations. WW3 historical time series (1976–2005) were shortened to the same range as buoy observations (1985–2005) and the missing times of observation measurements were removed from each model time series to better match the observed historical measurements.

Model performance was assessed by calculating mean absolute error (MAE) between modeled and observed H_{s95}, T_{p95}, and f_{ext} during DJF and JJA. f_{ext} was calculated for each year of modeled and observed time periods and the distribution of f_{ext} values was then compared using the MAE, as opposed to H_{s95} and T_{p95}, for which bulk data were used. MAE provides a measure of model accuracy when modeled and observed values are at approximately the same scale (Hyndman and Koehler, 2006) and is given by:

$$MAE = \frac{1}{N}\sum_{i=1}^{N}|obs_i - mod_i| \qquad (1)$$

where $obs_i = i^{th}$ observed value and $mod_i = i^{th}$ modeled value of the empirical cumulative density functions (CDFs) for DJF and JJA H_{s95}, T_{p95}, and f_{ext}. The MAE is not time dependent, and the gaps in the observation data had little effect on the assessment of H_{s95} and T_{p95} model error. So long as similar proportion of occurrences for each H_{s95} and T_{p95} value were represented, the incomplete observational dataset was sufficient to determine model error. Large gaps in the time series would affect calculation of f_{ext} model error. Therefore, years without 2 months of mostly temporally continuous (no gaps larger than 24 h) data were removed from the calculation of the MAE as outliers. Small gaps in the time series of a few hours were found to not significantly impact the calculation of f_{ext} and the MAE.

Model coherence was evaluated by calculating standard deviation of the mean (SDOM) of the multi-model average of H_{s95} and T_{p95} values for the historical period for DJF and JJA as:

$$SDOM = \frac{\sigma}{\sqrt{n}} \qquad (2)$$

where $\sigma =$ standard deviation calculated from the means of each model and $n =$ the number of sample means (within this study $n =$ 4, the number of means for each GCM driven WW3 output).

4. Results

4.1. Model Skill

Modeled H_{s95} reproduced observed H_{s95} and T_{p95} magnitudes well (Table 2). The H_{s95} DJF MAE was the smallest at buoy 51002, 0.28 m (6.1%), and the largest at buoy 51003, 0.53 m (11.5%). The 51003 MAE represented the largest error, but this MAE value was smaller than the calculated standard deviation of extreme wave heights. T_{p95} showed

Table 2

Average and standard deviation of H_{s95} and T_{p95} of observed values at selected NDBC stations within the Hawaiian Islands for 1985–2005 and MAE values calculated for multi-model hindcast H_{s95} and T_{p95}, at co-located WW3 virtual buoy output points by season. MAE statistics are represented in meters (seconds) and as a percentage of mean observed H_{s95} (T_{p95}).

Season	NDBC station	Averaged H_{s95} (m)	MAE H_{s95} (m)	(%)	Averaged T_{p95} (s)	MAE T_{p95} (s)	(%)
DJF	51002	4.53 ± 0.38	0.28	6.1	12.15 ± 3.20	1.61	13.2
	51003	4.60 ± 0.46	0.53	11.5	14.47 ± 4.93	1.30	9.0
	51004	4.52 ± 0.51	0.35	7.7	13.10 ± 3.19	1.73	13.2
JJA	51002	3.19 ± 0.39	0.18	5.6	9.33 ± 1.52	0.48	5.2
	51003	2.75 ± 0.38	0.50	18.2	9.73 ± 2.67	0.40	4.2
	51004	3.18 ± 0.53	0.40	12.5	9.97 ± 2.20	0.32	3.2

the opposite pattern, where buoy 51003 MAE was 1.30 s (9.0%). H_{s95} JJA MAE values were all less than or equal to 0.50 m, with buoy 51003 again being the largest at 0.50 m (18.1%). Buoy 51004 also showed a large MAE of 0.40 m (12.7%). JJA MAE values for T_{p95} were all less than 0.50 s (3.0–5.2%). Buoy 51003 likely had the largest H_{s95} error due to its location to the west of the Hawaiian Islands, whereby both DJF and JJA larger swell waves are refracted by the islands, leading to more variation between models and therefore error compared to historical observations. The H_{s95} and T_{p95} error statistics reported within this study are consistent with the range of similar studies that use dynamically-downscaled GCM-simulated winds to project wave climates (e.g., Hemer et al., 2013), though these statistics were for all wave parameters, not just the extremes. When calculating the MAE, the error values for the comparison time period (1985–2005) would be larger for H_{s95} and T_{p95} than for bulk H_s and T_p, as most non-extreme values were be similar. Therefore the error reported herein for the extremes within the range is considered acceptable and consistent with other studies, as the H_{s95} and T_{p95} error is within the range of errors reported for bulk H_s and T_p data.

The multi-model dataset did not approximate f_{ext} as well as H_{s95} and T_{p95} (Table 3). The largest DJF MAE values were 40 events/decade (24.1%) at NDBC station 51004 and 33 events/decade (18.5%). The largest JJA MAE was 33 events/season (25.5%) at station 51002. These larger errors indicate that the multi-model data set did not compare well to the observed datasets within these areas. Otherwise the remaining stations had smaller MAE (less than 15.0%). It should be noted, however, that the standard deviation of each observed location was larger than any MAE value. However, the model errors, being within one standard deviation of the observed mean, indicated that the even the locations with the largest errors present a possible distribution of events. Additionally, there is not a standard by which to define acceptable error for f_{ext}.

The multi-model dataset approximated DJF H_{s95} conditions well in the Hawaiian Islands, but was not as good a fit for JJA wave conditions (12.7% and 18.1% error for 51004 and 51003, respectively), with the models over-predicting wave magnitudes in both cases. Conversely,

Table 3

Average and standard deviation of f_{ext} of observed values at selected NDBC stations within the Hawaiian Islands for 1985–2005 and MAE values calculated for multi-model hindcast f_{ext}, at co-located WW3 virtual buoy output points by season. MAE statistics are represented in events/decade and as a percentage of mean observed f_{ext}.

Season	NDBC station	Averaged freq (Events/decade)	MAE fext (Events/decade)	(%)
DJF	51002	177.61 ± 68.50	32.78	18.5
	51003	153.81 ± 50.16	18.50	12.0
	51004	166.84 ± 64.61	40.22	24.1
JJA	51002	130.51 ± 46.64	33.33	25.5
	51003	128.37 ± 41.95	16.79	13.1
	51004	123.14 ± 47.49	7.17	5.8

T_{p95} was approximated well in JJA compared to DJF with smaller MAE values during these months. f_{ext} was not approximated well compared to the MAE percentages of H_{s95} and T_{p95} measurements, but the error was less than one standard deviation. Overall, the multi-model dataset acceptably simulated extreme wave conditions at these buoy locations. However, it should be noted that model skill in the Hawaiian Islands is not representative for the entire study area, since the accuracy of GCM-derived results can vary from region to region. The focus of this paper is to use relative changes between modeled historical and future wave conditions to discern trends and give a first-order analysis of implications for islands within the WTP.

H_{s95} SDOM was largest in the Marianas Region (0.30 m) (Fig. 1a). Additionally, extreme wave conditions were less consistent across GCM-forced model runs along the edges of the study area compared to the northern Central Region, the Eastern Equatorial Region, and the Main Hawaiian Islands. In all three regions, SDOM was less than 0.20 m. The western half of the study area represents the confluence of waves generated by the trade winds, Southern Hemisphere extratropical cyclones, and Northern Hemisphere extratropical cyclones. This convergence leads to large variation within each model due to the differing GCM physics and likely led to the moderate disagreement in H_{s95} between models. T_{p95} SDOM was often less than 1 s in magnitude and it was assumed that the T_{p95} coherence was generally good throughout the study area because of these small magnitudes (Fig. 1b). Changes of 1–2 s can reflect sizable differences in associated wave-driven run-up values, but the differences in T_{p95} values here are not large enough to indicate that resultant run-up values are significantly affected by model scatter. Overall, model coherence was deemed acceptable throughout the region and a multi-model average mutes individual model variation to more easily discern physical changes.

4.2. Wind speed and direction synopsis

Projected changes to trade wind speeds, the top 5% of wind speeds, and wind directions at island locations utilized in this research are reported in-depth in Storlazzi et al. (2015), and are briefly summarized here without analysis on broader meteorological patterns. Mean mid-century wind speed near the equator in all future scenarios did not change much with increased radiative forcing. Most average wind speed changes were less than 0.25 m/s and directions remained constant, travelling west to southwest. By the end-century, DJF averages decreased by 0.25 to 0.5 m/s in most regions within the study area under both scenarios with a larger decrease under RCP 8.5. This decrease is consistent with modeled wind speed projections documented by Dobrynin et al. (2012) and Lauer et al. (2013) for annual projections. JJA saw a small increase of 0.25–0.5 m/s in the Central Region islands with a similarly small decrease in wind speed intensity under RCP 8.5 in the Northeastern region.

Patterns of the means of the top 5% of wind speeds showed much more variability. The mean of the top 5% of RCP 4.5 and RCP 8.5 DJF wind speeds decrease throughout the century, with end-century decreases being 0.25–0.50 m/s and 0.25–0.75 m/s in most regions, respectively. The top 5% of JJA wind speeds increased by 0.25–0.75 m/s in the Central Region by 2100 in both scenarios with smaller decreases of 0.25–0.50 m/s in the Marianas region in RCP 4.5 and decreases of 0.25–0.75 m/s in the Marianas and Northeast Region in RCP 8.5. The mean directions of the top 5% of DJF wind speeds did not change noticeably in each scenario. JJA top 5% wind directions within the central region rotated clockwise by 5–10° in RCP 8.5 by 2100 and 10–20° under RCP 4.5.

4.3. Mid-century (2026–2045)

4.3.1. Mid-century: RCP 4.5

Mean H_{s95} was generally projected to decrease west of 180° within the study area and in the Southern Region. Decreases of approximately
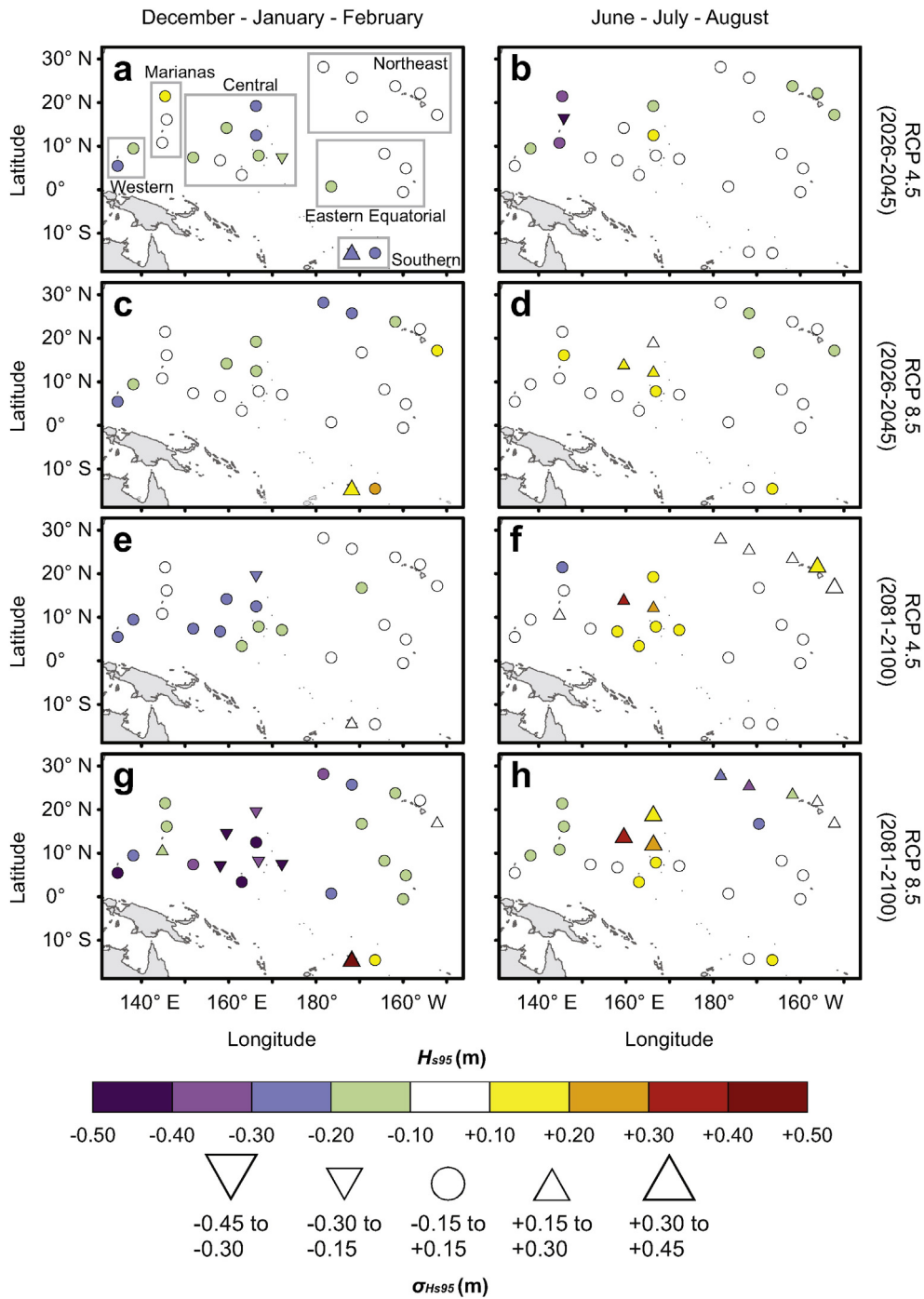
Fig. 2. Changes in ensemble H_{s95} and the change in σ_{Hs95} from hindcast (1976–2005) values. Change in 2026–2045 from hindcast for RCP 4.5 during (a) the DJF season, and (b) the JJA season. Change in 2026–2045 from hindcast for RCP 8.5 during (c) the DJF season, and (d) the JJA season. Change in 2081–2100 from hindcast for RCP 4.5 during (e) the DJF season, and (f) the JJA season. Change in 2081–2100 from hindcast for RCP 8.5 during (g) the DJF season, and (h) the JJA season. Colors represent change in H_{s95} in meters and shapes correspond to changes in σ_{Hs95}.

0.10–0.30 m (1.0–5.0%) in DJF H_{s95} compared to hindcast DJF values (see Supplementary Fig. 1a) were concentrated in the Central Region (Fig. 2a), but the Southern Region experienced a decrease in DJF H_{s95} of 0.20–0.30 m (5.0–7.0%). The only exception to this trend was at Asuncion where DJF H_{s95} increased by 0.11 m (4.1%). σ_{Hs95} did not change significantly throughout the study area, except at American Samoa, where it increased by 0.30 m (43.0%). JJA H_{s95} decreased primarily within the Marianas Region by approximately 0.30–0.45 m (7.0–9.0%) (Fig. 2b) compared to hindcast JJA values (see Supplementary Fig. 1b).

D_{m95} changes primarily occurred west of 180°, with the majority in the Central Region. DJF σ_{Dm95} increased by 5–15° at Palau, Pohnpei, Kosrae, and the Big Island of Hawaii, and by 16° at Chuuk (Fig. 3a). The largest DJF D_{m95} change (20° counterclockwise) occurred at American Samoa, accompanied by a small σ_{Dm95} decrease. JJA σ_{Dm95} decreased non-uniformly in the Central Region and at Howland by 5–10°, but showed a somewhat strong increasing trend of 5–15° in the Marianas Region and at Johnston Atoll (Fig. 3b). The greatest JJA D_{m95} shifts were in the Western and equatorial Central Regions, where D_{m95} rotated counter clockwise by approximately 15°.
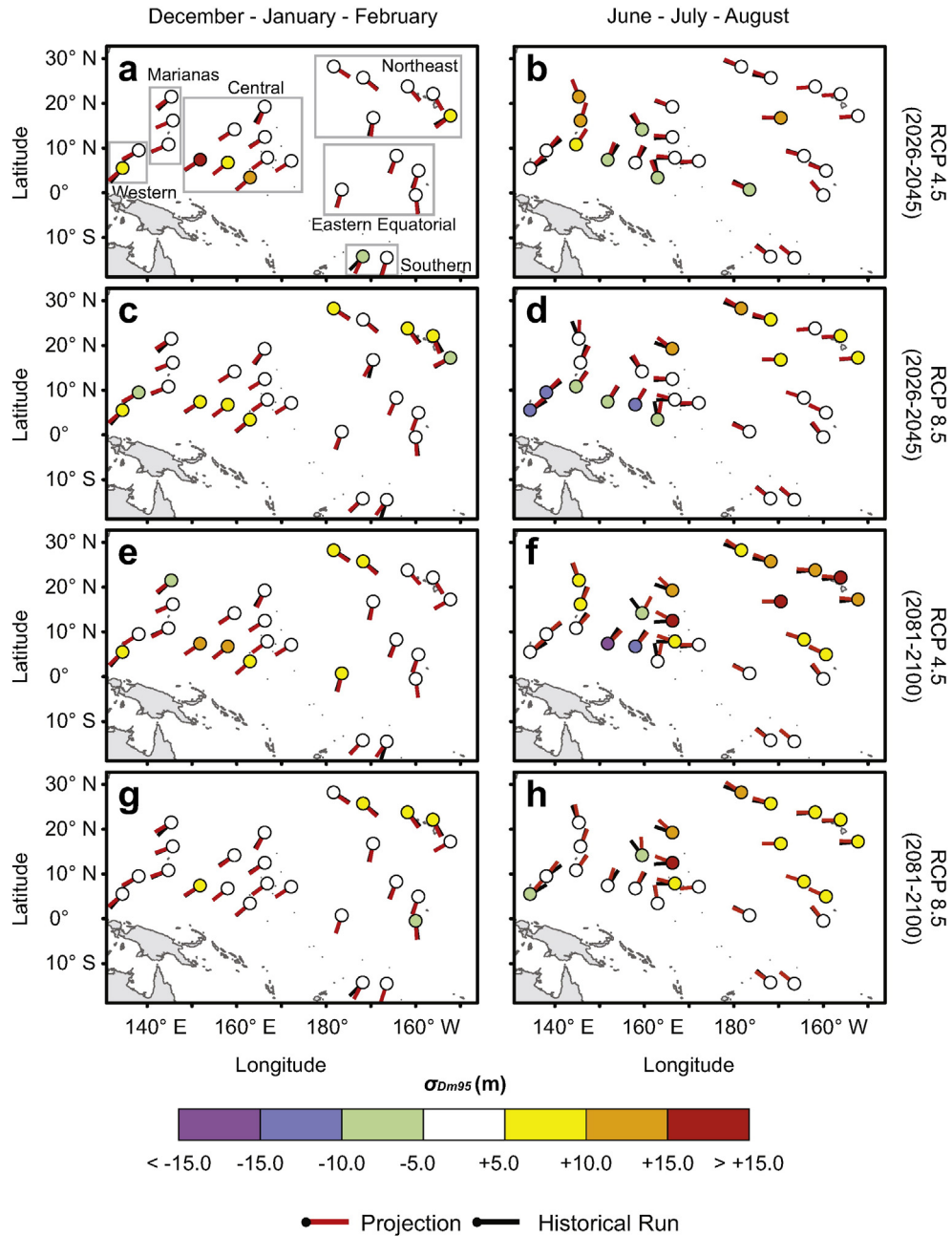
Fig. 3. Changes in ensemble D_{m95} and the change in σ_{Dm95} from hindcast (1976–2005) values. Change in 2026–2045 from hindcast for RCP 4.5 during (a) the DJF season, and (b) the JJA season. Change in 2026–2045 from hindcast for RCP 8.5 during (c) the DJF season, and (d) the JJA season. Change in 2081–2100 from hindcast for RCP 4.5 during (e) the DJF season, and (f) the JJA season. Change in 2081–2100 from hindcast for RCP 8.5 during (g) the DJF season, and (h) the JJA season. Black ticks indicate hindcast directions (D_{m95}), blue RCP 4.5 directions, and red RCP8.5 directions. Colors correspond to changes in σ_{Dm95}. Tick orientation indicates wave propagation towards island location.

Compared to hindcast frequencies, DJF f_{ext} non-uniformly increased north of 5° N by 5–15 events/decade (2.0–12.0%), with Wake (11.0%), Molokai (7.0%), and Midway (12.0%) featuring the largest departures (Fig. 4a). The only exception to this trend was at Kosrae, where f_{ext} decreased by 5–10 events/decade (6.5%). JJA f_{ext} showed similarly variable changes, with Howland having the largest decrease of 10–15 events/decade (12.0%) and Guam, Kosrae, and Kwajalein decreasing by 5–10 events/decade (8.0–10.0%) (Fig. 4b). The Big Island of Hawaii and Jarvis displayed an f_{ext} increase of 5–10 events/decade (6.0–7.0%). σ_f decreased at Kosrae, Kwajalein, Howland, and all Western Region islands.

4.3.2. Mid-century: RCP 8.5

Mean DJF H_{s95} was projected to generally decrease in the northern Central, western Northeast, and Western Regions by 0.10–0.30 m

(2.0–6.0%) (Fig. 2c) with the exception of the Big Island of Hawaii, which increased by 0.15 m (3.3%). DJF H_{s95} increased in the Southern Region by 0.10–0.30 m (5.0–16.0%), and σ_{Hs95} increased by 0.6 m (50.0%) at American Samoa. JJA H_{s95} values increased within the Central Region by 0.10–0.20 m (2.0–6.0%), accompanied by a small increase in σ_{Hs95} within its northern islands (Fig. 2d). The Northeast Region exhibited scattered decreases in H_{s95} of 0.10–0.20 m (3.0–4.0%).

DJF σ_{Dm95} generally increased at Palau, the Northeast Region, and equatorial islands in the Central Region by 5–10° with the exception of the Big Island of Hawaii where σ_{Dm95} decreased by 5–10° (Fig. 3c). This season did not exhibit many significant D_{m95} changes except at Johnston and Rose whereby values rotated approximately 15° clockwise. The majority of changes occurred during JJA. σ_{Hs95} decreased by 5–15° in Guam, the Western Region, and the equatorial Central Region
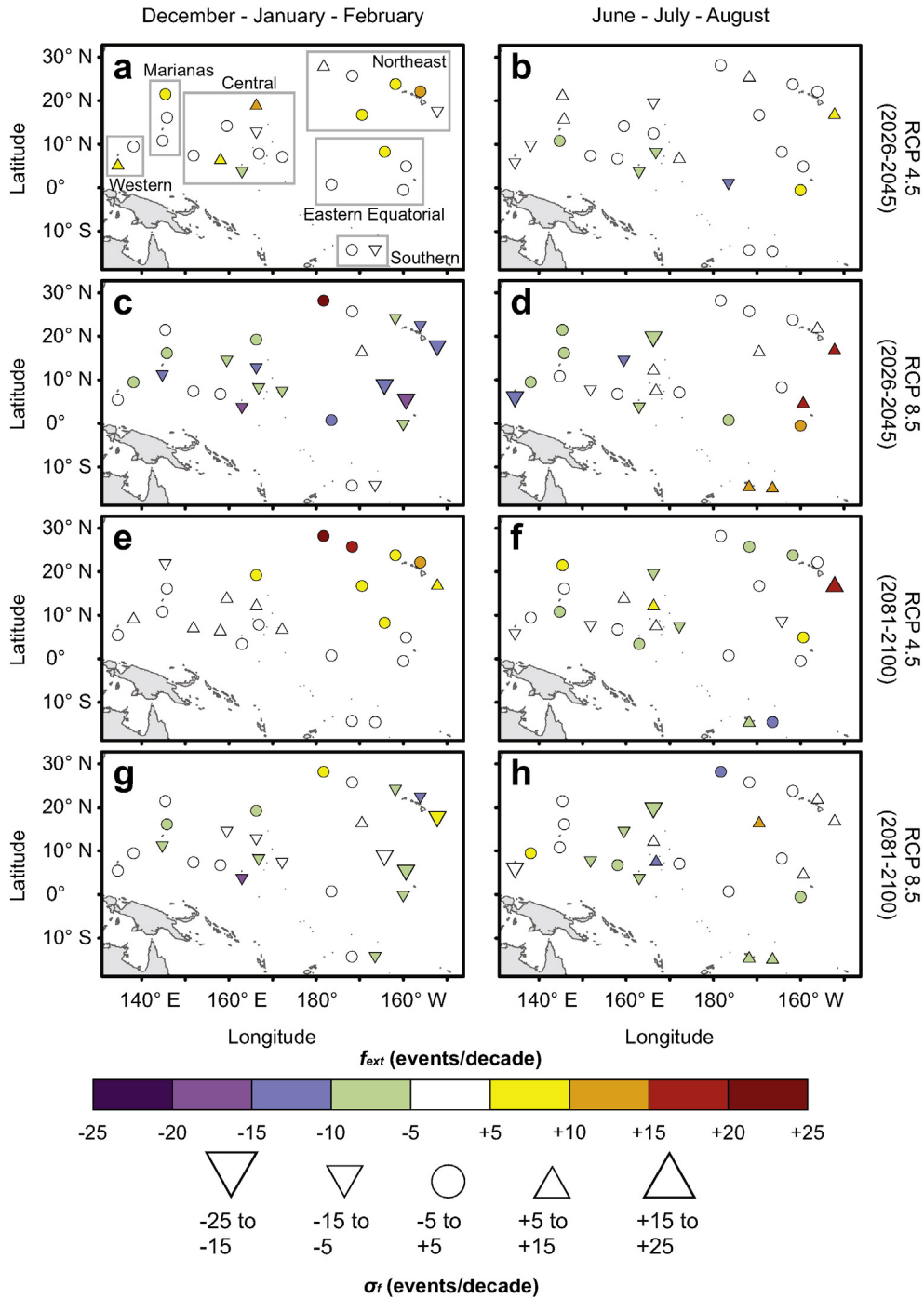
Fig. 4. Changes in ensemble f_{ext} and the change in σ_f from hindcast (1976–2005) values. Change in 2026–2045 from hindcast for RCP 4.5 during (a) the DJF season, and (b) the JJA season. Change in 2026–2045 from hindcast for RCP 8.5 during (c) the DJF season, and (d) the JJA season. Change in 2081–2100 from hindcast for RCP 4.5 during (e) the DJF season, and (f) the JJA season. Change in 2081–2100 from hindcast for RCP 8.5 during (g) the DJF season, and (h) the JJA season. Colors represent change in f_{ext} in events/decade and shapes correspond to changes in σ_f.

islands (Fig. 3d). σ_{Hs95} increased in the Northeastern Region and at Wake by 5–15°. The largest D_{m95} changes during this season were at Asuncion, Kosrae, and Wake, each rotating clockwise by approximately 20°.

DJF f_{ext} decreased for the most part at every region except for Midway, Johnston, the Northwest Hawaiian Islands, and the Southern Region islands (Fig. 4c). The largest decreases were at Kosrae and Palmyra, each decreasing by 15–20 events/decade (13.0–16.0%). Midway's f_{ext} increased by 22 events/decade (12.8%). σ_f at most islands decreased from hindcast values, with the greatest decreases (15–25 events/decade [30.0–32.0%]) at the Big Island of Hawaii, Kingman

Reef, and Palmyra Atoll. JJA f_{ext} generally increased in the far eastern part of the study area, especially at Palmyra Atoll and the Big Island of Hawaii (Fig. 4d). f_{ext} decreased in the Western Region, the northern Marianas Region, and at Wake, Enewetak, Kosrae, and Howland, with most points showing a decrease of 5–10 events/decade (7.0–13.0%) and Enewetak and Palau decreasing by 10–15 events/decade (13.7% and 13.0%, respectively). σ_f increased east of 107° E by 5–15 events/decade (2.0–30.0%), except at Wake. σ_f decreases characterized the western remainder of the study area, with the strongest decreases at Palau and Wake. These trends, however, were weak and non-uniform for each area.

4.4. End-century (2081–2100)

4.4.1. End-century: RCP 4.5

The majority of projected DJF changes in H_{s95} occurred west of 180°, with the Central and Western Regions displaying decreases of 0.10–0.30 m (3.0–7.0%) (Fig. 2e). As opposed to mid-century values, JJA H_{s95} values increased within the Central Region; the largest increases were at Enewetak (0.32 m [10.0%]) and Bikini (0.23 m [7.5%]) (Fig. 2f). Both islands and the majority of the Northeast islands experienced an increase in σ_{Hs95}, with the easternmost Hawaiian Islands showing the largest change.

DJF σ_{Dm95} displayed a small increase (5–15°) in the equatorial Central Region islands of Kosrae, Pohnpei, and Chuuk as well as at Howland, Palau, Midway, and the Northwest Hawaiian Islands (Fig. 3e). In general, these changes were similar to the patterns present in both mid-century scenarios. D_{m95} did not change significantly except at Rose, where it rotated clockwise 17°. JJA σ_{Dm95} increased east of 160° E, north of 5° N, and in the northern Marianas Region (Fig. 3f). The largest increases were at Molokai (~17°), Johnston Atoll (~17°), and Bikini (~30°). σ_{Dm95} decreased at Enewetak, Pohnpei, and Chuuk by approximately 20°. The largest D_{m95} changes occurred in the Central Region, specifically at Bikini (clockwise 33°), Enewetak (clockwise 66°), Wake (clockwise 25°), Kwajalein (clockwise 19°), and Kosrae (clockwise 21°).

Every Northeast Region island, Wake, and Kingman Reef showed an increase in DJF f_{ext}. Midway and the Northwest Hawaiian Islands exhibited the largest change of 15–20 events/decade (8.0–14.0%) and the trend became stronger progressing northeast (Fig. 4e). σ_f increased in the Central Region and at Yap despite no significant changes in f_{ext}. JJA f_{ext} trends were inconsistent, with only the Southern Region clearly defined by a decrease in f_{ext} at both locations (Fig. 4f). The largest increase was at the Big Island of Hawaii (20 events/decade [6.0%]), but other islands within the region had small decreases of 5–10 events decade (Kauai [6.1%] and the Northwest Hawaiian Islands [8.6%]) or showed no significant change. Similarly, σ_f changes were not consistent across the study area, with Palau, Chuuk, Wake, Majuro, and Kingman Reef decreasing while Enewetak, Kwajalein, American Samoa, and the Big Island of Hawaii increased.

4.4.2. End-Century: RCP 8.5

Projected H_{s95} were similar to RCP 4.5 trends, but tended to be greater in magnitude and more widespread. DJF decreases affected every region except the Southern Region (Fig. 2g). The mean H_{s95} of most points within the Northern Hemisphere decreased by more than 0.30 m, with the strongest decreases in the Central Region of approximately 0.45 m (11.0%). Decreased H_{s95} at these islands was often accompanied by a 0.15–0.30 m (30.0–40.0%) decrease in σ_{Hs95}. The H_{s95} increased by 0.46 m (13.3%) at American Samoa and by 0.13 m at Rose (3.2%), with the σ_{Hs95} of American Samoa increasing by 0.30–0.45 m. JJA patterns exhibited an increase in Central Region H_{s95} values of 0.10 to more than 0.30 m (3.0–10.0%), and the largest increases were at Enewetak (0.32 m [9.7%]) and Bikini Atoll (0.23 m [7.6%]) (Fig. 2h). H_{s95} decreased throughout the surrounding regions. H_{s95} decreased by 0.10–0.20 m (2.0–4.0%) in the Marianas Region, by 0.10–0.30 m (5.0–10.0%) in the western Northeast Region islands, and by 0.35 m (10.0%) at the Northwest Hawaiian Islands. Similar to RCP 4.5, σ_{Hs95} increased in the northern Central Region and the Northeast Region, with the largest increases occurring at Enewetak, Bikini, and Wake. The similarity between the two end-century scenarios was in contrast to the differences in mid-century scenarios. Boreal winter values were projected to undergo the largest changes in both scenarios.

DJF σ_{Dm95} did not change significantly except in the Northern Hawaiian Islands and at Chuuk, where values increased by 5–10° and Jarvis, where σ_{Dm95} decreased by 5–10° (Fig. 3g). The largest changes in D_{m95} were at Asuncion (clockwise 15.0°) and American Samoa (counter-clockwise 15.0°). JJA σ_{Dm95} followed a similar increasing pattern within most Northern Hemisphere islands east of 160°, but increased

by 5–10° (Fig. 3h). σ_{Dm95} at Bikini had the largest increase (15°). JJA σ_{Dm95} decreased by 5–10° at Enewetak and Palau. The Central Region islands displayed a clockwise D_{m95} shift of about 15°. Though smaller than the RCP 4.5 scenario, shifts in D_{m95} were again largest at Enewetak (35°) and Bikini (26°).

DJF f_{ext} decreased weakly by 5–10 events/decade at many islands and strongly (15–20 events/decade [16.8%]) at Kosare. At the Big Island of Hawaii and Midway, f_{ext} increased by 5–10 events/decade (5.7% and 4.1%, respectively) (Fig. 4g). Otherwise f_{ext} showed no significant trend. f_{ext} at Kosrae and Molokai decreased by the largest amounts: 16 (17.0%) and 14 events/decade (9.0%), respectively. σ_f similarly decreased across the study area, with stronger, more consistent decreases to the east. JJA f_{ext} decreased within the Central and Southern Regions (Fig. 4h). Again these decreases were small, generally less than 10 events/decade (5.0–10.0%). The Northwest Hawaiian Islands and Jarvis also saw decreases of 5–10 events/decade (5.2% and 8.7% respectively) while Yap and Johnston had increases of 5–15 events/decade (7.4% and 12.2% respectively). σ_f decreased within the Central Region and at Palau. There was a small increase in σ_f (5–15 events/decade [15.0–30.0%]) in the easternmost islands, at Johnston, and in the Southern Region.

4.5. Statistical Significance

Statistical significance of H_{s95} trends was assessed by fitting a least-squares linear regression line to yearly averages of the seasonal concatenated H_{s95} data for hindcast, mid-century, and end-century periods. The significance of the regression trend was assessed using an F-test with the null hypothesis that the regression slope is zero and an alternative hypothesis that the slope is significant at the 95% confidence level (Emery and Thomson, 2001; See Supplemental Material: Significance Tests). Effectively, if the trend is determined to be significant, then the forecast data is interpreted as significantly different (higher or lower) than the hindcast data. The significance of the H_{s95} regression model was assessed for each radiative forcing scenario and for the DJF and JJA seasons. The DJF RCP 8.5 H_{s95} trends significantly decreased at Midway, Chuuk, Asuncion, Kosrae, Palau, Pohnpei, Yap, Majuro, Enewetak, Bikini, the Northwest Hawaiian Islands, Kwajalein, Wake, Johnston, Kingman Reef, Palmyra, Howland, and Jarvis over the century. The DJF RCP 4.5 H_{s95} decreasing trend was significant at Chuuk, Kosrae, Palau, Pohnpei, Enewetak, Bikini, Kwajalein, and Wake.

JJA H_{s95} trends for both RCP 4.5 and RCP 8.5 were mostly not significant. The JJA RCP 8.5 H_{s95} trend significantly decreased at Kauai, Midway, the Northwest Hawaiian Islands, and Johnston. The JJA H_{s95} RCP 4.5 decreasing trend was statistically significant at Jarvis, though the mean values decreased by less than 0.10 m. The increase of H_{s95} during JJA at the Central region islands was not significant. As the standard deviations of H_{s95} increased by the end of the century, there was a worse fit of a least-squares trend line, effectively demonstrating no significant change.

The statistical significance of the changes in D_{m95} was assessed by comparing the directional distributions of the hindcast, mid-century, and end-century periods using a directional Kuiper test at the 95% confidence level (Stephens, 1965; Marida and Jupp, 2009; See supplemental Material: Significance Tests). The change in mid-century RCP 4.5 DJF D_{m95} from hindcast was significant at the Big Island of Hawaii, Chuuk, Yap, Johnston, and Howland. The mid-century DJF D_{m95} change was statistically significant at Asuncion, Palau, Molokai, and Kingman Reef. Mid-century RCP 4.5 JJA D_{m95} changed significantly at the Big Island of Hawaii, Chuuk, Asuncion, Yap, Enewetak, Kingman Reef, and Rose. Mid-century RCP 4.5 JJA D_{m95} changed significantly at Chuuk, Saipan, Asuncion, Palau, Yap, the Northwest Hawaiian Islands, Wake, Rose, and Jarvis.

End-century RCP 4.5 DJF D_{m95} changed significantly at American Samoa, Saipan, Molokai, Wake, Johnston, and Rose. End-century RCP 8.5 DJF D_{m95} significantly rotated at American Samoa, Saipan, Palau,

Yap, Guam, Wake, and Howland. End-century changes in RCP 4.5 JJA D_{m95} were significant at Kauai, Chuuk, Saipan, Kosrae, Palau, Pohnpei, Enewetak, Bikini, Molokai, the Northwest Hawaiian Islands, Kwajalein, Howland, and Jarvis. End-century RCP 8.5 JJA D_{m95} changed significantly at Kauai, the Big Island of Hawaii, Chuuk, Asuncion, Palau, Yap, Enewetak, Bikini, Molokai, Wake, Howland, and Jarvis.

f_{ext} changes were found, in all instances, to not be statistically significant. In general, many of the changes in f_{ext} tended to be small (generally < 16%) with only a few locations seeing a change of 25 events/decade. However, the changes observed may not necessarily be noise in the data. To adequately assess whether these changes signify an (admittedly) weak trend or noise, a larger forecast period (past 2100) will need to be simulated. These small projected changes can have larger ramifications by slightly increasing/decreasing the risk of a larger wave event coinciding with transient high sea levels.

5. Discussion

5.1. Comparison with previous studies

Most studies of mean and extreme Pacific Ocean wave climate projections in recent years have been part of larger, global-scale studies, and many only offer changes to annual means. Present model results are broadly consistent with the results from these studies under various climate change scenarios.

Hemer et al. (2013) and Semedo et al. (2013) projected that mean boreal winter H_s decreased in the western Pacific by as much as 10%, consistent with the results presented herein whereby many of the largest changes in H_{s95} at island locations decreased by 7–11% with smaller decreases throughout the entire region (Fig. 2e, g). Similarly, Fan et al. (2014) projected a small decrease in swell and wind sea energy density west of Hawaii during the this season and Wang et al. (2014) found a decrease in maximum H_s within the region by 0.15–0.30 m under RCP 8.5 by the end of the century. The magnitudes of DJF decrease under RCP 8.5 reported in this study were as much as 0.45 m at some locations, but followed the same broad decreasing trend. Additionally, Mori et al. (2010, 2013) describe annual-scale changes to H_s averages on a global scale under climate change, projecting 0.05–0.10 m decrease in annual means. While these values are for annual means, the boreal winter is typically the most energetic season and likely dominates annual averages. Comparing these results with the end-century winter values, the decrease in wave heights west of Hawaii is still discernible, despite the different averaging scales.

JJA trends differed from Hemer et al. (2013) July–September projections within the Central Region. Their projections show a weak decreasing trend in wave heights by less than 5% whereas Fig. 2(f, h) demonstrate an increase in H_{s95} by as much as ~10% (0.32 m) within this region, consistent with Semedo et al. (2013). Conversely, Wang et al. (2014) reported a small increase in mean and maximum July–September H_s of west of the Hawaiian Islands by as much as 0.15–0.30 m, which is within the range of reported increases within the Central Region. Similarly, they reported a decrease in mean H_s near Hawaii that is also represented in our JJA RCP 8.5 result (Fig. 2h).

DJF directions are projected to broadly remained unchanged, often changing by less than 5° (Fig. 3), which is supported by Hemer et al. (2013) and Fan et al. (2014), where wave directions during this season did not change significantly. The greatest differences observed between studies in boreal summer wave directions were within the central region. Hemer et al. (2013) projected little change in wave directions within this region while Fan et al. (2014) demonstrated that July–September sea and swell wave directions within the region rotate clockwise in response to climate change, with the swell becoming oriented almost directly north. Fig. 3(f, h) similarly denote a clockwise rotation in Dm_{95} for many of the islands west of 180°. The frequency of large wave events within the WTP has not been previously reported, and a

discussion of potential causes of frequency changes are listed in the following section.

5.2. Potential Cause of Changes in Extreme Waves

Under both RCP 4.5 and 8.5 for the mid-century and end-century, DJF H_{s95} is projected to decrease throughout much of the study area, likely driven by changes to the intensity and frequency of North Pacific extratropical cyclones. It is generally agreed that there will be poleward shifts in storm tracks and resultant wave energy under warming conditions (Bengtsson et al., 2006; Ulbrich et al., 2008; Catto et al., 2011; Wu et al., 2011; Semedo et al., 2013) and that these shifts will be accompanied by decreased frequency of storm events within the extratropics (Bengtsson et al., 2006; Chang et al., 2012; Eichler et al., 2013). As the DJF wave climates of the central Pacific are greatly influenced by swell from the north Pacific storms (Alves, 2006; Semedo et al., 2011), the projected decrease in DJF H_{s95} in the Northern Hemisphere are attributed to the poleward shifts of storm tracks and reduced storm frequency. The reduction of the frequency of north Pacific storm events and the decrease of wave period and swell energy within the northwest Pacific in response to climate change (Hemer et al., 2013; Fan et al., 2014) accounts for the lower mean DJF values reported within his study. Similarly, projected increases in end-century JJA H_{s95} likely result from increased Southern Hemisphere storm intensity, generating large swell that arrives at the Central Region islands (Bengtsson et al., 2006). A future study will need to analyze the pressure fields of the four GCM forcings used in this study to determine the magnitude of changes to storm tracks or storm frequency under the radiative forcing scenarios. However, it is beyond the scope of this study to ascertain the broader meteorological/climatological trends of storms and pressure fields through the Pacific over the 21st century. Therefore, the results are presented within the context of other studies of storm tracks, swell, and wave magnitude changes.

Changes in end-century JJA D_{m95} likely result from changes in the types of waves that dominate Central Region islands during boreal summer months. Historical mean wave directions demonstrate that Central Region islands receive most JJA wave energy from trade wind waves from the east (Fig. 3b), with Southern Hemisphere swell becoming more dominant progressing west through the region, as can be seen by the broad clockwise rotation of D_{m95} (Fig. 3). Southern Ocean extratropical cyclone swell waves can influence areas well into the Northern Hemisphere and dramatically affect local wave climates of the WTP (Young, 1999; Alves, 2006; Semedo et al., 2011). Clockwise shifts in wave direction at some of the Central islands suggests that, relative to trade wind seas, Southern Hemisphere swell will contribute more to extreme incident waves in the future compared to historical conditions. Fan et al. (2014) documented a strong increase in projected southern Pacific swell energy density during the boreal summer, accompanied by a clockwise rotation of mean swell propagation direction within the central Pacific with climate change. The clockwise rotation of mean D_{m95} within the Central Region indicates a similar pattern, whereby increasing swell energy from the south will generate larger waves within the Central Region compared to today, despite projected increases to trade wind strength (and, by extension, waves) under climate changes as demonstrated by Merrifield (2011) and Merrifield and Maltrud (2011). The resultant directional shifts could dramatically alter the erosional patterns of the shorelines of both atoll and high islands. Mid-century RCP 4.5 DJF H_{s95} at the Big Island of Hawaii increased by 0.10–0.20 m compared with Midway, the Northeast Hawaiian Islands, and Kauai, where H_{s95} decreased by 0.10–0.30 m. A possible cause for this difference within the region could stem from increased energy in the generation region of larger swell that reaches the Big Island. The DJF D_{m95} for the location is broadly to the southwest, very different from the other locations, whose waves propagate towards the southeast. This increase compared to others could be due to an increase in storminess in the northeastern Pacific (Eichler et al., 2013), which

would affect the Big Island of Hawaii's wave heights, but not necessarily the other Northeast Region Islands that receive the most of their DJF energy from the northwest.

f_{ext} results showed much varying trends between mid- and end-centuries for each forcing scenario. Mid-century DJF RCP 8.5 trends show the largest general decrease in f_{ext} by as much as 20 events/decade in the Northern Hemisphere, following the trend of decreasing northern hemisphere storm frequency (Bengtsson et al., 2006; Chang et al., 2012; Eichler et al., 2013). By the end-century, while there is a very weak decreasing trend, it is not as strong as during the mid-century period. The smaller magnitudes of change indicate possible changes to these storm frequencies between mid- and end-century, whereby there is a relative increase in storminess relative to the mid-century period, though this finding would be at odds with the trends of Bengtsson et al. (2006); Chang et al. (2012), and Eichler et al. (2013). The smaller magnitudes of change indicate possible changes to these storm frequencies between mid- and end-century, whereby there is a relative increase in storminess relative to the mid-century period. However, under climate change, Catto et al. (2011) noted greater storm track density in the northeastern Pacific extratropics under four times present CO_2 levels compared to a two times CO_2 levels scenario during the DJF season. This increase in frequency coupled with an eastward shift in the high storm density regions can account for the difference between frequencies. In both cases, the shifts cause a decrease in DJF large wave event frequency compared to present, but increasing storm frequency under the higher climate change scenario (reflecting greater radiative forcing during the end-century) in the northeast Pacific would likely drive smaller than mid-century changes. This change is not reflected in the H_{s95} values for the DJF season, indicating that the incident waves may be smaller as a result of this shift. The increase of 15–25 events/decade in DJF f_{ext} in the Northeast Region projected under RCP 4.5 for both mid- and end-centuries reflects increases in linear storm tack frequency trends for RCP 4.5 in the northeastern Pacific observed by Eichler et al. (2013) that were not present for RCP 8.5. The increase in storminess in the northeastern Pacific can result in an increased frequency of swell from this region reaching the islands of the Northeast Region (Alves, 2006). JJA changes were mainly attributed to changes in trade wind intensity and southern hemisphere storminess. Under most scenarios, f_{ext} decreased weakly throughout the study region, with the largest exception being the eastern islands under RCP 8.5. The general decrease here is attributed to the poleward shift of and decrease in the number of extratropical storms in the southern hemisphere, and therefore the instances of large swell that these storms generate (Bengtsson et al., 2006). These above trends are not applicable everywhere. Mid-century RCP 4.5 DJF f_{ext} for Midway increased by 25 events/decade in contrast to most other regions seeing a decrease. This difference could be due to Midway's position (being the most northern island in the study area) whereby it receives more frequent waves compared to the remainder of the study area due to storm proximity. Similarly, there is an increase in the eastern islands' f_{ext} during the JJA season during the mid-century RCP 4.5 scenario as well as the Big Island of Hawaii's f_{ext} by 2100. The rest of the Northeast region does not change dramatically, but the Big Island point's f_{ext} increases by 15–20 events/decade by 2100. It is currently unclear as to what the true drivers of the smaller scale variability could be. Therefore, further research into storm systems changes within the GCM pressure fields would need to address why these locations are singularly different during these time periods.

5.3. Implications for island sustainability

H_{s95} is projected to decrease throughout the mid- to western tropical Pacific during DJF throughout the 21st century under both RCP 4.5 and 8.5, with the largest decreases occurring within the Central Region by as much as 0.45 m (12.0%). Wave driven set-up along reef flats and run-up levels onshore would therefore be smaller (Becker et al., 2014, see Section 2.3). Furthermore, the decrease in σ_{Hs95} under RCP 8.5 by

2100 in the Central Region indicates that H_{s95} would be consistently lower. However, with sea levels increasing by approximately 0.5–1.5 m by 2100 (Vermeer and Rahmstorf, 2009; Church et al., 2013), the effects of the projected decrease in H_{s95} will be muted and more energy will propagate to shore relative to the historical period. Increased energy at the shoreline will drive stronger reef flat currents that could result in enhanced coastal erosion (Storlazzi et al., 2011; Grady et al., 2013). Additionally, vertical reef flat accretion at atolls and fringing reefs is anticipated to be negligible due to slower growth rates compared to projected SLR rates (Buddemeier and Smith, 1988; Montaggioni, 2005), reducing the effectiveness of these reefs as a buffer for these reef-lined island shorelines into the future. More inundation and more sediment resuspension from large waves propagating onto the reef flat are certain with SLR (Storlazzi et al., 2011). The results of this study suggest that projected DJF run-up and longshore current strength along island shorelines will not be as great in magnitude throughout the Central Region, where end-century wave heights decrease by as much as 12.0% under RCP 8.5 and 7.0% under RCP 4.5 compared to using contemporary H_{s95} values to project future values under SLR (Fig. 1e, g).. JJA run-up will increase considerably in the Central Region by the end of the century under both climate change scenarios as increased H_{s95} of as much as 10% (Fig. 1f, h) will increase wave-driven set-up along reefs, reducing depth-limited breaking and increasing inland flooding and longshore drift magnitudes. Consequently, morphological changes of these quasi-equilibrated shorelines will be more dramatic compared to present. Increasing JJA H_{s95} at the Central Region islands coupled with SLR will drive more extensive flooding of these islands during this season.

Atoll island erosional patterns will change due to increasing wave heights and SLR, but the dominant control on island morphodynamic change is the magnitude of wave direction change. Changing wave directions in turn alters longshore current strength and possibly direction (Kench et al., 2009). The D_{m95} rotation of 15–30° in the Central Region islands (Fig. 3f, h) could drive large shifts in coastline erosional patterns and alter longshore current intensity (Kench et al., 2009). Atoll island shorelines vary considerably over shorter time scales in response to changing wave directions and shorelines can migrate several meters over a few years under new conditions (Rankey, 2011). The projected clockwise rotation of JJA D_{m95} by 30–40° in the Central Region in some locations (Fig. 3f) will cause incident waves to arrive along parts of the island coastlines that are currently not subject to larger wave events, or at least not to events of that frequency or magnitude. Historical run JJA D_{m95} within the Central Region propagated toward the west to northwest. By 2100, JJA D_{m95} under both climate scenarios is markedly different at Wake, Bikini, and Enewetak, with dominant waves travelling to the northwest to north. A D_{m95} shift of 20° could result in rapid shoreline adjustment and new erosional patterns, which would threaten island communities, especially on urbanized or human-altered islands where current extrema induce flooding and damage to infrastructure (Yamano et al., 2007; Ford, 2012). Seasonal changes in wave direction can cause significant fluctuation in atoll island shorelines; for example, Kench and Brander (2006) found that Maldivian atoll shorelines can change considerably between monsoon seasons. Therefore, the large variation in D_{m95} by 2100 between DJF and JJA at many islands, especially Enewetak and Bikini, could result in significant inter-seasonal oscillations in island shoreline areas.

f_{ext} changes can impact islands in two ways. First, a long-term increase in the frequency of large H_s events on the order of 10 events/decade, as projected for the Northeast Region under RCP 4.5 (Fig. 4e) can alter shoreline erosion patterns by increasing episodes of strong longshore drift and the number of flooding episodes. A decrease in f_{ext} would result in the opposite pattern: fewer large erosional episodes and less frequent flooding. Second, an increase in frequency also increases the likelihood that one of these events will coincide with other contributors to anomalously high water levels (e.g., King tides or ENSO). Under RCP 4.5, DJF f_{ext} increased by 15–20 events/decade

(8.0–14.0%) over the 21st century in the Northeast Region. Combined with little to no change in H_{s95} under this scenario and increasing SLR, it is likely that the increase will drive larger and more frequent flooding along these island shorelines. An atoll island aquifer can take months to a year to freshen after a large flooding event (Terry and Falkland, 2010), and more frequent flooding from the DJF f_{ext} increase projected in the Northeast Region (Fig. 4) may create conditions where the islands' freshwater resources are brackish for extended periods. JJA RCP 4.5 f_{ext} decreased by 5–10 events/decade (1.0–10.0%) throughout the Northern Hemisphere, but the changes were spatially scattered. Possible future damage and hazards posed to Central islands from SLR will be somewhat mitigated, as it is less likely that large waves will coincide with transient high sea levels. DJF f_{ext} under RCP 8.5 decreased largely by mid-century, by 5–20 events/decade (1.0–14.0%) throughout most regions (Fig. 4c), and the likelihood that large wave events will occur simultaneously with temporary high sea levels will decrease. Therefore, it seems that under RCP 8.5, aside from SLR, the potential risk for large swell events to cause significant onshore damage will decrease compared to current conditions as H_{s95} will decrease by 0.20–0.40 m throughout the Northern Hemisphere regions, indicating reduced set-up and flooding potential, and the most energetic of these waves each season will become somewhat less frequent throughout the study area.

6. Conclusions

Coastal flooding risk will increase within the WTP due to SLR; changes in the WTP wave climate during the 21st century will modulate the magnitude and frequency of flooding. The trends observed under RCP 8.5 are an intensification of similar trends observed under RCP 4.5, except for f_{ext}. It is apparent, and expected, that a greater amount of radiative forcing (RCP 8.5) will result in the strongest changes. Under RCP 8.5, H_{s95} within the WTP during DJF will become smaller and less frequent. It is therefore possible that RCP 8.5 boreal winter waves in particular may become less hazardous as large waves will less frequently coincide with King tides or ENSO-driven water levels. Regardless, the decrease in f_{ext} will reduce any anticipated wave-driven modification of island shorelines as there will be less incident wave energy arriving at island coastlines. The biggest divergence is the increase in DJF f_{ext} in the Northeast Region under RCP 4.5, possibly leading to more flooding and more erosion of island shorelines. The large D_{m95} changes seen during JJA will also lead to dramatic shifts in island morphology and potentially damage infrastructure under both scenarios.

The projected decreases in H_{s95} during DJF, the season that typically delivers the most wave energy, throughout the study area by 2100 do not indicate that these islands will be safe from inundation. A decrease in H_{s95} results in less set-up and therefore less energy reaching island shorelines, assuming no changes to local sea level. However, even conservative estimates of SLR project a global increase of 0.50 m by 2100 (Church et al., 2013), so island shorelines will be subject to more incident wave energy regardless of changes in wave climate. Future flooding events will inevitably be larger and more frequent, affecting a larger inland area. However, the DJF H_{s95} we project indicates that flooding events and morphological changes to islands will not be as severe as if hindcast values are assumed to couple with SLR. Conversely, the large JJA D_{m95} rotations at both end-century scenarios coupled with increased sea levels and increased H_{s95} within the Central Region will drive large changes to island shorelines that will threaten infrastructure.

Future studies will need to create a more detailed picture of the changing wave climates within the WTP and the effects these changes will have on island morphologies and populations. Although the results from this study generally correlate with the changes in wave climates published by other studies (Semedo et al., 2011; Hemer et al., 2013; Fan et al., 2014), it will be important for future studies to incorporate larger multi-model ensembles of GCMs to increase result robustness. This study focused on extratropical cyclone and trade wind swell, but

high water levels associated with tropical cyclones will be a necessary addition to modeling future hazards to island communities. Additionally, hazard projections will have to take into account changing f_{ext}, which has not been discussed previously. The current DJF 10-year flooding event will become more frequent due to SLR, but larger 50–100-year events that depend on the synergy of large waves and other temporally elevated sea levels are projected to become rarer under RCP 8.5 throughout the WTP. Under RCP 4.5 this trend reverses within the Northeastern Region, where the extreme events are projected become more frequent. Otherwise, the uncertain nature of how atoll islands will respond to both rapid SLR and changing wave climates over the next century will also need to be addressed. The coral reef flats make run-up from large events by empirical relationships likely inaccurate due to wave energy reductions and changing bathymetry. Therefore it will be necessary to employ high-resolution, nearshore, hydrodynamic models to ascertain island response to the changing wave conditions presented here. Overall, the future effects of extratropical storm swell on tropical Pacific islands will be island-specific and accurate individual island response models will require detailed bathymetries and in situ ground truthing measurements.

Supplementary data to this article can be found online at http://dx.doi.org/10.1016/j.gloplacha.2016.03.009.

References

Alves, J., 2006. Numerical modelling of ocean swell contributions to the global wind-wave climate. Ocean Model. 11 (1-2), 98–122. http://dx.doi.org/10.1016/j.ocemod.2004.11.007.

Aucan, J., Hoeke, R., Merrifield, M.A., 2012. Wave-driven sea level anomalies at the Midway tide gauge as an index of North Pacific storminess over the past 60 years: NORTH PACIFIC STORMINESS. Geophys. Res. Lett. 39, 1–6. http://dx.doi.org/10.1029/2012GL052993.

Australian Bureau of Meteorology and CSIRO, 2014. Climate Variability, Extremes and Change in the Western Tropical Pacific: New Science and Updated Country Reports. Pacific-Australia Climate Change Science and Adaptation Planning Program Technical Report. Australian Bureau of Meteorology and Commonwealth Scientific and Industrial Research Organisation, Melbourne, Australia.

Becker, J.M., Merrifield, M.A., Ford, M., 2014. Water level effects on breaking wave setup for Pacific Island fringing reefs. J. Geophys. Res. Oceans 119, 914–932. http://dx.doi.org/10.1002/2013JC009373.

Beetham, E.P., Kench, P.S., 2014. Wave energy gradients and shoreline change on Vabbinfaru platform, Maldives. Geomorphology 209, 98–110. http://dx.doi.org/10.1016/j.geomorph.2013.11.029.

Bengtsson, L., Hodges, K.I., Roeckner, E., 2006. Storm tracks and climate change. J. Clim. 19, 3518–3543.

Bromirski, P.D., Cayan, D.R., Helly, J., Wittmann, P., 2013. Wave power variability and trends across the North Pacific. J. Geophys. Res. Oceans 118, 6329–6348. http://dx.doi.org/10.1002/2013JC009189.

Buddemeier, R.W., Smith, S.V., 1988. Coral reef growth in an era of rapidly rising sea level: predictions and suggestions for long-term research. Coral Reefs 7, 51–56.

Catto, J.L., Shaffrey, L.C., Hodges, K.I., 2011. Northern hemisphere extratropical cyclones in a warming climate in the HiGEM high-resolution climate model. J. Clim. 24, 5336–5352. http://dx.doi.org/10.1175/2011JCLI4181.1.

Chang, E., Guo, Y., Xia, X., 2012. CMIP5 multimodel ensemble projection of storm track change under global warming. J. Geophys. Res. 117 (D23), 1–19. http://dx.doi.org/10.1029/2012JD018578.

Church, J.A., White, N.J., Hunter, J.R., 2006. Sea-level rise at tropical Pacific and Indian Ocean islands. Glob. Planet. Chang. 53, 155–168. http://dx.doi.org/10.1016/j.gloplacha.2006.04.001.

Church, J.A., Clark, P.U., Cazenave, A., Gregory, J.M., Jevrejeva, S., Levermann, A., Merrifield, M.A., Milne, G.A., Nerem, R.S., Nunn, P.D., Payne, A.J., Pfeffer, W.T., Stammer, D., Unnikrishnan, A.S., 2013. Sea Level Change. In: Stocker, T.F., Qin, D., Plattner, G.-K.,

Tignor, M., Allen, S.K., Boschung, J., Nauels, A., Xia, Y., Bex, V., Midgley, P.M. (Eds.), Climate Change 2013: The Physical Science Basis. Contribution of Working Group I to the Fifth Assessment Report of the Intergovernmental Panel on Climate Change. Cambridge University Press, Cambridge, United Kingdom and New York, NY, USA.

Dickinson, W.R., 1999. Holocene sea-level record on Funafuti and potential impact of global warming on central Pacific atolls. Quat. Res. 51, 124–132. http://dx.doi.org/10.1006/qres.1998.2029.

Dobrynin, M., Murawsky, J., Yang, S., 2012. Evolution of the global wind wave climate in CMIP5 experiments. Geophys. Res. Lett. 39 (18), 1–6. http://dx.doi.org/10.1029/2012GL052843.

Donat, M., Leckebusch, G., Wild, S., Ulbrich, U., 2010. Benefits and limitations of regional multi-model ensembles for storm loss estimations. Clim. Res. 44, 211–225. http://dx.doi.org/10.3354/cr00891.

Eichler, T., Gaggini, N., Pan, Z., 2013. Impacts of global warming on Northern Hemisphere winter storm tracks in the CMIP5 model suite. J. Geophys. Res. 118 (10), 3919–3932. http://dx.doi.org/10.1002/jgrd.50286.

Emery, W.J., Thomson, R.E., 2001. Data Analysis Methods in Physical Oceanography. second ed. Elsevier Science B.V., New York, New York, USA, p. 638.

Fan, Y., Held, I.M., Lin, S.J., Wang, X.L., 2013. Ocean Warming Effect on Surface Gravity Wave Climate Change for the End of the Twenty-First Century. J. Clim. 26, 6046–6066. http://dx.doi.org/10.1175/JCLI-D-12-00410.1.

Fan, Y., Lin, S.J., Griffies, S.M., Hemer, M.A., 2014. Simulated global swell and wind-sea climate and their responses to anthropogenic climate change at the end of the twenty-first century. J. Clim. 27, 3516–3536. http://dx.doi.org/10.1175/JCLI-D-13-00198.1.

Ferrario, F., Beck, M.W., Storlazzi, C.D., Micheli, F., Shepard, C.C., Airoldi, L., 2014. The effectiveness of coral reefs for coastal hazard risk reduction and adaptation. Nat. Commun. 5. http://dx.doi.org/10.1038/ncomms4794.

Fletcher, C.H., Richmond, B.M., 2010. Climate change in the Federated States of Micronesia: Food and water security, climate risk management, and adaptive strategies. University of Hawaii Sea Grant Report TT-10-02, 32.

Ford, M., 2012. Shoreline changes on an urban atoll in the central Pacific Ocean: Majuro Atoll, Marshall Islands. J. Coast. Res. 279, 11–22. http://dx.doi.org/10.2112/JCOASTRES-D-11-00008.1.

Grady, A.E., Moore, L.J., Storlazzi, C.D., Elias, E., Reidenbach, M.A., 2013. The influence of sea level rise and changes in fringing reef morphology on gradients in alongshore sediment transport. Geophys. Res. Lett. 40, 3096–3101. http://dx.doi.org/10.1002/grl.50577.

Hasselmann, S., Hasselmann, K., Allender, J.H, Barnett, T.P., 1985. Computations and parameterizations of the nonlinear energy transfer in gravity-wave spectrum. Part I: a new method for efficient computations if the exact nonlinear transfer integral. J. Phys. Oceanogr. 15, 1369–1377.

Hemer, M.A., Fan, Y., Mori, N., Semedo, A., Wang, X.L., 2013. Projected changes in wave climate from a multi-model ensemble. Nat. Clim. Change. 3, 471–476. http://dx.doi.org/10.1038/nclimate1791.

Hoeke, R.K., McInnes, K.L., Kruger, J.C., McNaught, R.J., Hunter, J.R., Smithers, S.G., 2013. Widespread inundation of Pacific islands triggered by distant-source wind-waves. Glob. Planet. Chang. 108, 128–138. http://dx.doi.org/10.1016/j.gloplacha.2013.06.006.

Hyndman, R.J., Koehler, A.B., 2006. Another look at measures of forecast accuracy. Int. J. Forecast. 22, 679–688. http://dx.doi.org/10.1016/j.ijforecast.2006.03.001.

Kench, P.S., Brander, R.W., 2006. Response of reef island shorelines to seasonal climate oscillations: South Maalhosmadulu atoll, Maldives. J. Geophys. Res. 111. http://dx.doi.org/10.1029/2005JF000323.

Kench, P.S., Parnell, K.E., Brander, R.W., 2009. Monsoonally influenced circulation around coral reef islands and seasonal dynamics of reef island shorelines. Mar. Geol. 266, 91–108. http://dx.doi.org/10.1016/j.margeo.2009.07.013.

Kim, S., Yu, J., 2012. The two types of ENSO in CMIP5 models. Geophys. Res. Lett. 39 (11), 1–6. http://dx.doi.org/10.1029/2012GL052006.

Lauer, A., Zhang, C., Elison-Timm, O., 2013. Downscaling of climate change in the Hawaii region using CMIP5 results: on the choice of forcing fields. J. Clim. 26 (24), 10006–10030. http://dx.doi.org/10.1175/JCLI-D-13-00126.1.

Marida, K.V., Jupp, P.E., 2009. Directional Statistics. John Wiley and Sons, Ltd, New York, New York, USA, p. 460.

Merrifield, M.A., 2011. A shift in western tropical Pacific Sea level trends during the 1990s. J. Clim. 24, 4126–4138. http://dx.doi.org/10.1175/2011JCLI3932.1.

Merrifield, M.A., Maltrud, M.E., 2011. Regional sea level trends due to a Pacific trade wind intensification: SEA LEVEL AND PACIFIC TRADE WINDS. Geophys. Res. Lett. 38. http://dx.doi.org/10.1029/2011GL04957 (n/a–n/a).

Merrifield, M.A., Becker, J.M., Ford, M., Yao, Y., 2014. Observations and estimates of wave-driven water level extremes at the Marshall Islands. Geophys. Res. Lett. 41, 7245–7253. http://dx.doi.org/10.1002/2014GL061005.

Mimura, N., 1999. Vulnerability of island countries in the South Pacific to sea level rise and climate change. Clim. Res. 12, 137–143.

Montaggioni, L.F., 2005. History of Indo-Pacific coral reef systems since the last glaciation: development patterns and controlling factors. Earth Sci. Rev. 71, 1–71.

Mori, N., Yasuda, T., Mase, H., Tom, T., Oku, Y., 2010. Projection of extreme wave climate change under global warming. Hydrol. Res. Lett. 4, 15–19. http://dx.doi.org/10.3178/hrl.4.15.

Mori, N., Shimura, T., Yasuda, T., Mase, H., 2013. Multi-model climate projections of ocean surface variables under different climate scenarios—future change of waves, sea level and wind. Ocean Eng. 71, 122–129. http://dx.doi.org/10.1016/j.oceaneng.2013.02.016.

National Data Buoy Center (NDBC), 2013. National oceanic and atmospheric administration online data. URL: http://www.ndbc.noaa.gov.

National Geophysical Data Center, 2013. Global self-consistent hierarchical high-resolution geography database version 2.2.2 online data. URL: http://www.ngdc.noaa.gov/mgg/shorelines/gshhs.html.

Naval Research Laboratory, 2013. Digital Bathymetric Database version 3.0 online data. URL: http://www7320.nrlssc.navy.mil/DBDB2_WWW/v3.0/NRLCOM_dbdb2.html.

Nicholls, R.J., Wong, P.P., Burkett, V.R., Codignotto, J.O., Hay, J.E., McLean, R.F., Ragoonaden, S., Woodroffe, C.D., 2007. Coastal systems and low-lying areas. In: Parry, M.L., Canziani, O.F., Palutikof, J.P., van der Linden, P.J., Hanson, C.E. (Eds.), Climate Change 2007: Impacts, Adaptation and Vulnerability. Contribution of Working Group II to the Fourth Assessment Report of the Intergovernmental Panel on Climate Change. Cambridge University Press, Cambridge, UK, pp. 315–356.

Pequignet, A.C., Becker, J.M., Merrifield, M.A., Boc, S.J., 2011. The dissipation of wind wave energy across a fringing reef at Ipan. Guam. Coral Reefs 36 (3), 71–82.

Rankey, E.C., 2011. Nature and stability of atoll island shorelines: Gilbert Island chain, Kiribati, equatorial Pacific: atoll shoreline change, equatorial Pacific. Sedimentology 58, 1831–1859. http://dx.doi.org/10.1111/j.1365-3091.2011.01241.x.

Riahi, K., Krey, V., Rao, S., Chirkov, V., Fischer, G., Kolp, P., Kindermann, G., Nakicenovic, N., Rafai, P., 2010. RCP-8.5: exploring the consequence of high emission trajectories. Clim. Chang. 109 (1-2), 33–57.

Rotzoll, K., Fletcher, C.H., 2012. Assessment of groundwater inundation as a consequence of sea-level rise. Nat. Clim. Chang. 3, 477–481. http://dx.doi.org/10.1038/nclimate1725.

Semedo, A., Sušelj, K., Rutgersson, A., Sterl, A., 2011. A global view on the wind sea and swell climate and variability from ERA-40. J. Clim. 24, 1461–1479. http://dx.doi.org/10.1175/2010JCLI3718.1.

Semedo, A., Weisse, R., Behrens, A., Sterl, A., Bengtsson, L., Günther, H., 2013. Projection of global wave climate change toward the end of the twenty-first century. J. Clim. 26 (21), 8269–8288. http://dx.doi.org/10.1175/JCLI-D-12-00658.1.

Seneviratne, S.I., Nicholls, N., Easterling, D., Goodess, C.M., Kanae, S., Kossin, J., Luo, Y., Marengo, J., McInnes, K., Rahimi, M., Reichstein, M., Sorteberg, A., Vera, C., Zhang, X., 2012. Changes in climate extremes and their impacts on the natural physical environment. In: Field, C.B., Barros, V., Stocker, T.F., Qin, D., Dokken, D.J., Ebi, K.L., Mastrandrea, M.D., Mach, K.J., Plattner, G.-K., Allen, S.K., Tignor, M., Midgley, P.M. (Eds.), Managing the Risks of Extreme Events and Disasters to Advance Climate Change AdaptationA Special Report of Working Groups I and II of the Intergovernmental Panel on Climate Change (IPCC). Cambridge University Press, Cambridge, UK, and New York, NY, USA, pp. 109–230.

Smithers, S.G., Hoeke, R.K., 2014. Geomorphological impacts of high-latitude storm waves on low-latitude reef islands — observations of the December 2008 event on Nukutoa, Takuu, Papua New Guinea. Geomorphology 222, 106–121. http://dx.doi.org/10.1016/j.geomorph.2014.03.042.

Stephens, M.A., 1965. The goodness-of-fit statistic V_N: distribution and significance points. Biometrics 52 (3–4), 309–321.

Stevenson, S., 2012. Significant changes to ENSO strength and impacts in the twenty-first century: results from CMIP5. Geophys. Res. Lett. 39 (17), 1–5. http://dx.doi.org/10.1029/2012GL052759.

Storlazzi, C.D., Elias, E., Field, M.E., Presto, M.K., 2011. Numerical modeling of the impact of sea-level rise on fringing coral reef hydrodynamics and sediment transport. Coral Reefs 30, 83–96. http://dx.doi.org/10.1007/s00338-011-0723-9.

Storlazzi, C.D., Shope, J.B., Erikson, L.H., Hegermiller, C.A., Barnard, P.L., 2015. Future wave and wind projections for United States and United States-affiliated Pacific Islands. U.S. Geological Survey Open-File Report 2015–1001, p. 426 http://dx.doi.org/10.3133/ofr20151001.

Terry, J.P., Falkland, A.C., 2010. Responses of atoll freshwater lenses to storm-surge overwash in the Northern Cook Islands. Hydrogeol. J. 18, 749–759. http://dx.doi.org/10.1007/s10040-009-0544-x.

Thomson, A.M., Calvin, K.V., Smith, S.J., Kyle, G.P., Volke, A., Patel, P., Delgado-Arias, S., Bond-Lamberty, B., Wise, M.A., Clarke, L.E., Edmonds, J.A., 2011. RCP4.5: a pathway for stabilization of radiative forcing by 2100. Clim. Chang. 109, 77–94. http://dx.doi.org/10.1007/s10584-011-0151-4.

Tolman, H.L., 2009. User manual and system documentation of WAVEWATCH III version 3.14. NOAA/NWS/NCEP/MMAB Technical Note 276, p. 19.

Tolman, H.L., Balasubramaniyan, B., Burroughs, L.D., Chalikov, D.V., Chao, Y.Y, Chen, H.S., Gerald, V.M., 2002. Development and implementation of win-generated ocean surface wave models at NCEP. Weather Forecast 17 (2), 311–333.

Tolman, H.L., Chalikov, D.V., 1996. Source terms in a third-generation win wave model. J. Phys. Oceanogr. 26, 2497–2518.

Ulbrich, U., Pinto, J.G., Kupfer, H., Leckebusch, G.C., Spangehl, T., Reyers, M., 2008. Changing northern hemisphere storm tracks in an ensemble of IPCC climate change simulations. J. Clim. 21, 1669–1679. http://dx.doi.org/10.1175/2007JCLI1992.1.

Vermeer, M., Rahmstorf, S., 2009. Global sea level linked to global temperature. Proc. Natl. Acad. Sci. 106, 21527–21532.

Vitousek, S., Fletcher, C.H., 2008. Maximum annually recurring wave heights in Hawai'i 1. Pac. Sci. 62, 541–553.

Wang, X., Swail, V., Cox, A., 2009. Dynamical versus statistical downscaling methods for ocean wave heights. Int. J. Climatol. 30 (3), 317–332. http://dx.doi.org/10.1002/joc.1899.

Wang, X.L., Feng, Y., Swail, V.R., 2014. Changes in global ocean wave heights as projected using multimodel CMIP5 simulations. Geophys. Res. Lett. 41 (3), 1026–1034. http://dx.doi.org/10.1002/2013GL058650.

Webb, A.P., Kench, P.S., 2010. The dynamic response of reef islands to sea-level rise: evidence from multi-decadal analysis of island change in the Central Pacific. Glob. Planet. Chang. 72, 234–246. http://dx.doi.org/10.1016/j.gloplacha.2010.05.003.

Woodroffe, C.D., 2008. Reef-island topography and the vulnerability of atolls to sea-level rise. Glob. Planet. Chang. 62, 77–96. http://dx.doi.org/10.1016/j.gloplacha.2007.11.001.

World Climate Research Programme, 2013. CMIP5 — coupled model intercomparison project phase 5 overview. URL: http://cmip-pcmdi.llnl.gov/cmip5/.

Wu, Y., Ting, M., Seager, R., Huang, H., Cane, M.A., 2011. Changes in storm tracks and energy transports in a warmer climate simulated by the GFDL CM2.1 model. Clim. Dyn. 3 (1–2), 53–72. http://dx.doi.org/10.1007/s00382-010-0776-4.

Yamano, H., Kayanne, H., Yamaguchi, T., Kuwahara, Y., Yokoki, H., Shimazaki, H., Chikamori, M., 2007. Atoll island vulnerability to flooding and inundation revealed by historical reconstruction: Fongafale Islet, Funafuti Atoll, Tuvalu. Glob. Planet. Chang. 57, 407–416. http://dx.doi.org/10.1016/j.gloplacha.2007.02.007.

Young, I.R., 1999. Seasonal variability of the global ocean wind and wave climate. Int. J. Climatol. 19, 931–950.